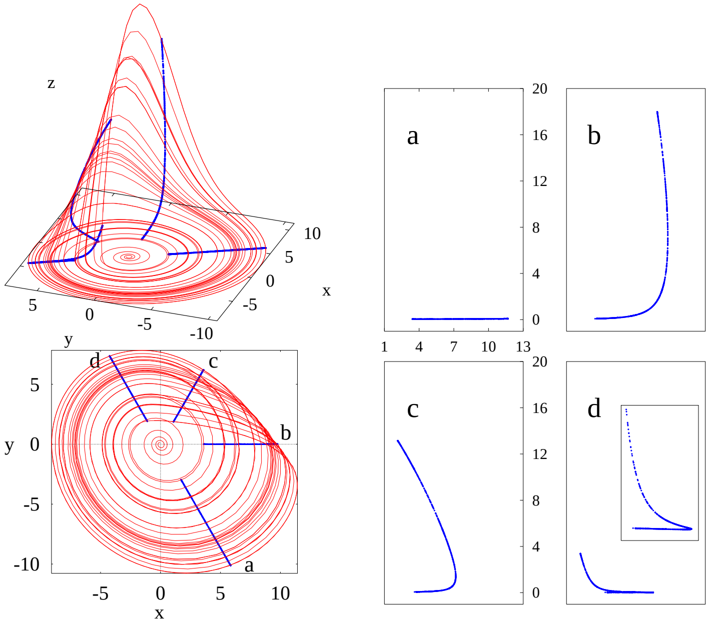

Figure 3.1: (Right:) a sequence of Poincaré sections of the Rössler strange attractor, defined by planes through the z axis, oriented at angles (a) -60^o (b) 0^o, (c) 60^o, (d) 120^o, in the x-y plane. (Left:) side and x-y plane view of trajectory with Poincaré sections superimposed. (Rytis Paškauskas)

Duffing oscillator
Rossler@Rössler system

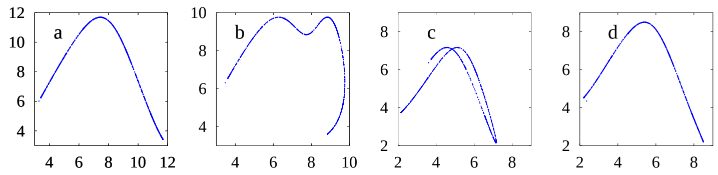

Figure 3.2: Return maps for the $R_n \to R_{n+1}$ radial distance Poincaré sections of figure 3.1. (Rytis Paškauskas)

Example 3.2 Pendulum: *The phase space of a simple pendulum is 2-dimensional: momentum on the vertical axis and position on the horizontal axis. We choose the Poincaré section to be the positive horizontal axis. Now imagine what happens as a point traces a trajectory through this phase space. As long as the motion is oscillatory, in the pendulum all orbits are loops, so any trajectory will periodically intersect the line, that is the Poincaré section, at one point.*

Consider next a pendulum with friction, such as the unforced Duffing system plotted in figure 2.2. Now every trajectory is an inward spiral, and the trajectory will intersect the Poincaré section $y = 0$ at a series of points that get closer and closer to either of the equilibrium points; the Duffing oscillator at rest.

Motion of a pendulum is so simple that you can sketch it yourself on a piece of paper. The next two examples offer a better illustration of the utility of visualization of dynamics by means of Poincaré sections.

Example 3.3 Rössler attractor: *Consider figure 2.3, a typical trajectory of the 3-dimensional Rössler flow (2.12). It wraps around the z axis, so a good choice for a Poincaré section is a plane passing through the z axis. A sequence of such Poincaré sections placed radially at increasing angles with respect to the x axis, figure 3.1, illustrates the "stretch & fold" action of the Rössler flow. To orient yourself, compare this with figure 2.3, and note the different z-axis scales. Figure 3.1 assembles these sections into a series of snapshots of the flow. A line segment $[A, B]$, traversing the width of the attractor, starts out close to the x-y plane, and after the stretching (a) $\to$ (b) followed by the folding (c) $\to$ (d), the folded segment returns close to the x-y plane strongly compressed. In one Poincaré return the $[A, B]$ interval is stretched, folded and mapped onto itself, so the flow is expanding. It is also mixing, as in one Poincaré return the point C from the interior of the attractor is mapped into the outer edge, while the edge point B lands in the interior.*

Once a particular Poincaré section is picked, we can also exhibit the return map (3.1), as in figure 3.2. Cases (a) and (d) are examples of nice 1-to-1 return maps. However, (b) and (c) appear multimodal and non-invertible, artifacts of projections of a 2-dimensional return map $(R_n, z_n) \to (R_{n+1}, z_{n+1})$ onto a 1-dimensional subspace $R_n \to R_{n+1}$.

make axes legible in figure 3.2

The dynamics of high-dimensional flows, such as a truncation of the infinite tower of the Kuramoto-Sivashinsky modes (2.19) can be difficult to visualize. The question is: how is one to look at such a flow? It is not clear that restricting the dynamics to a Poincaré section necessarily helps - after all, a section reduces a $(d+1)$-dimensional flow to a d-dimensional map, and how much is gained by replacing a continuous flow in 16 dimensionas by a

Kuramoto-Sivashinsky system

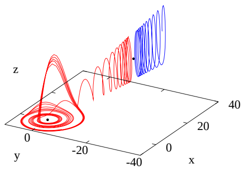

Figure 4.3: Two trajectories of the Rössler flow initiated in the neighborhood of the "+" equilibrium point (4.26). (R. Paškauskas)

The two equilibria together their stability exponents now yield quite detailed information about the flow. Figure 4.3 shows two trajectories which start in the neighborhood of the "+" equilibrium point. Trajectories to the right of the "+" equilibrium point escape, and those to the left spiral toward the "−" equilibrium point, where they seem to wander chaoticaly for all times. The stable manifold of "+" equilibrium point thus serves as a attraction basin boundary. Consider now the linearized stability exponents of the two equilibria

2.9 page 49

$$\begin{array}{rcll}(\lambda_1^-, \lambda_2^- \pm i\,\theta_2^-) &=& (\,-5.686, & 0.0970 \pm i\,0.9951\,) \\ (\lambda_1^+, \lambda_2^+ \pm i\,\theta_2^+) &=& (\,0.1929, & -4.596\times 10^{-6} \pm i\,5.428\,)\end{array} \qquad (4.27)$$

The $\lambda_2^+ \pm i\,\theta_2^+$ complex eigenvalue pair implies that that neighborhood of the outer equilibrium point rotates with angular period $T_+ \approx \left|2\pi/\theta_2^+\right| = 1.1575$. The stability multiplier by which a trajectory that starts near the "+" equilibrium point contracts in the stable manifold plane is the excrutiatingly slow $\Lambda_2^+ \approx \exp(\lambda_2^+ T_+) = 0.9999947$ per rotation, while moving away along the unstable eigendirection by factor $\Lambda_1^+ \approx \exp(\lambda_1^+ T_+) = 1.2497$. Hence the slow spiraling on both sides of the "+" equilibrium point.

The $\lambda_2^- \pm i\,\theta_2^-$ complex eigenvalue pair tells us that neighborhood of the "−" equilibrium point rotates with angular period $T_- \approx \left|2\pi/\theta_2^-\right| = 6.3135$. The stability multiplier by which a trajectory that starts near the "−" equilibrium point spirals away per one rotation is $\Lambda_{radial} \approx \exp(\lambda_2^- T_-) = 1.84$, all the while being contracted into the stable manifold by the amazing factor of $\Lambda_z \approx \exp(\lambda_1^- T_-) = 10^{-15.6}$ (!).

Suppose you start with a 1 mm interval pointing in the z direction. After one Poincaré return the interval is of order of 10^{-4} fermi, *the furthest we will get into subnuclear structure in this book. Of course, from the mathematical point of view, the flow is reversible, and the Poincaré return map is invertible.*

Example 4.7 **Why does a flame front flutter?** *The Kuramoto-Sivashinsky flat flame front $u(x,t) = 0$ is an equilibrium point of (2.16). The matrix of variations (4.3) follows from (2.19)*

$$A_{kj}(a) = \frac{\partial v_k(x)}{\partial a_j} = (k^2 - \nu k^4)\delta_{kj} - 2ka_{k-j}\,. \qquad (4.28)$$

For the $u(x,t) = 0$ equilibrium solution the matrix of variations is diagonal, and – as in (4.14) – so is the Jacobian matrix $\mathbf{J}^t_{kj}(0) = \delta_{kj} e^{(k^2-\nu k^4)t}$.

Lyapunov exponent!equilibrium
Euler!limit

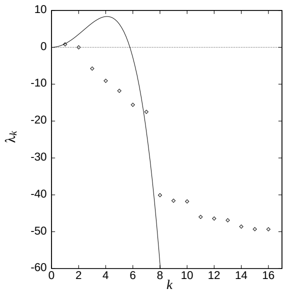

Figure 4.4: Lyapunov exponents $\lambda_{\overline{1},k}$ versus k for the least unstable spatio-temporally periodic orbit $\overline{1}$ of the Kuramoto-Sivashinsky system, compared with the stability exponents of the $u(x,t) = 0$ stationary solution, $\lambda_k = k^2 - \nu k^4$. The eigenvalue $\lambda_{\overline{1},k}$ for $k \geq 8$ falls below the numerical accuracy of integration and are not meaningful. $N = 16$ Fourier mode truncation, $\nu = 0.029924$. The cycle $\overline{1}$ was computed using methods of chapter 17. (From ref. [2.10])

For $\nu > 1$, $u(x,t) = 0$ is the globally attractive stable equilibrium. As the "viscosity" decreases below $\nu \leq 1$, the dynamics goes through a rich sequence of bifurcations on which we shall not dwell here. The $|k| < 1/\sqrt{\nu}$ long wavelength perturbations of the flat-front equilibrium are linearly unstable, while all $|k| > 1/\sqrt{\nu}$ short wavelength perturbations are strongly contractive. The high k eigenvalues, corresponding to rapid variations of the flame front, decay so fast that the corresponding eigendirections are physicallly irrelevant. To illustrate the rapid contraction in the non-leading eigendirections we plot in figure 4.4 the eigenvalues of the equilibrium in the unstable regime, for relatively low viscosity ν, and compare them with the stability eigenvalues of the least unstable cycle for the same value of ν. The equilibrium solution is very unstable, in 5 eigendirections, the least unstable cycle only in one. Note that for $k > 7$ the rate of contraction is so strong that higher eigendirections are numerically meaningless for either solution; even though the flow is infinite-dimensional, the attracting set must be rather thin.

4.3.2 Stability of trajectories

Next, consider the case of a general, non-stationary trajectory $x(t)$. The exponential of a constant matrix can be defined either by its Taylor series expansion, or in terms of the Euler limit (4.13):

appendix M.1

$$e^{t\mathbf{A}} = \sum_{k=0}^{\infty} \frac{t^k}{k!}\mathbf{A}^k \qquad (4.29)$$

$$= \lim_{m\to\infty}\left(\mathbf{1} + \frac{t}{m}\mathbf{A}\right)^m . \qquad (4.30)$$

Taylor expanding is fine if $\mathbf{A}$ is a constant matrix. However, only the second, tax-accountant's discrete step definition of an exponential is appropriate for the task at hand, as for a dynamical system the local rate of neighborhood distortion $\mathbf{A}(x)$ depends on where we are along the trajectory. The linearized neighborhood is multiplicatively deformed along the flow, and the m discrete time step approximation to $\mathbf{J}^t$ is therefore given by a generalization of the Euler product (4.30):

$$\begin{aligned}\mathbf{J}^t &= \lim_{m\to\infty}\prod_{n=m}^{1}(\mathbf{1} + \delta t\mathbf{A}(x_n)) = \lim_{m\to\infty}\prod_{n=m}^{1} e^{\delta t\,\mathbf{A}(x_n)} \qquad (4.31)\\ &= \lim_{m\to\infty} e^{\delta t\,\mathbf{A}(x_n)} e^{\delta t\,\mathbf{A}(x_{m-1})} \cdots e^{\delta t\,\mathbf{A}(x_2)} e^{\delta t\,\mathbf{A}(x_1)}\,,\end{aligned}$$

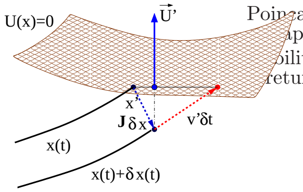

Poincar"'e!return map!stability
stability!Poincar"'e return map

Figure 4.5: If $x(t)$ intersects the Poincaré section $\mathcal{P}$ at time τ, the nearby $x(t) + \delta x(t)$ trajectory intersects it time $\tau + \delta t$ later. As $(U' \cdot v'\delta t) = -(U' \cdot \mathbf{J}\,\delta x)$, the difference in arrival times is given by $\delta t = -(U' \cdot \mathbf{J}\,\delta x)/(U' \cdot v')$.

4.4.1 Stability of Poincaré return maps

(R. Paškauskas and P. Cvitanović)

We now relate the linear stability of the Poincaré return map $P : \mathcal{P} \to \mathcal{P}$ defined in sect. 3.1 to the stability of the continuous time flow in the full phase space.

The hypersurface $\mathcal{P}$ can be specified implicitly through a function $U(x)$ that is zero whenever a point x is on the Poincaré section. A nearby point $x + \delta x$ is in the hypersurface $\mathcal{P}$ if $U(x + \delta x) = 0$, and the same is true for variations around the first return point $x' = x(\tau)$, so expanding $U(x')$ to linear order in δx leads to the condition

$$U_i(x') \left.\frac{dx'_i}{dx_j}\right|_{\mathcal{P}} = 0\,. \tag{4.40}$$

In what follows U_i is the gradient of U defined in (3.2), unprimed quantities refer to the starting point $x = x_0 \in \mathcal{P}$, $v = v(x_0)$, and the primed quantities to the first return: $x' = x(\tau)$, $v' = v(x')$, $U' = U(x')$. For brevity we shall also denote the full phase space Jacobian matrix at the first return by $\mathbf{J} = \mathbf{J}^\tau(x_0)$. Both the first return x' and the time of flight to the next Poincaré section $\tau(x)$ depend on the starting point x, so the Jacobian matrix

$$\hat{\mathbf{J}}(x)_{ij} = \left.\frac{dx'_i}{dx_j}\right|_{\mathcal{P}} \tag{4.41}$$

with both initial and the final variation constrained to the Poincaré section hypersurface $\mathcal{P}$ is related to the continuous flow Jacobian matrix by

$$\left.\frac{dx'_i}{dx_j}\right|_{\mathcal{P}} = \frac{\partial x'_i}{\partial x_j} + \frac{dx'_i}{dt}\frac{dt}{dx_j} = \mathbf{J}_{ij} + v'_i \frac{dt}{dx_j}\,.$$

The return time variation dt/dx, figure 4.5, is eliminated by substituting this expression into the constraint (4.40),

$$0 = U'_i\,\mathbf{J}_{ij} + (v' \cdot U')\frac{dt}{dx_j}\,,$$

singular value decomposition

⇓PRELIMINARY

⇑PRELIMINARY

redraw figure

yielding the projection of the full space $(d+1)$-dimensional Jacobian matrix to the Poincaré map d-dimensional Jacobian matrix:

$$\hat{\mathbf{J}}_{ij} = \left(\delta_{ik} - \frac{v'_i\,U'_k}{(v' \cdot U')}\right)\mathbf{J}_{kj}\,. \tag{4.42}$$

Substituting (4.6) we verify that the initial velocity $v(x)$ is a zero-eigenvector of $\hat{\mathbf{J}}$

$$\hat{\mathbf{J}} v = 0\,, \tag{4.43}$$

so the Poincaré section eliminates variations parallel to v, and $\hat{\mathbf{J}}$ is a rank d matrix, that is, one less than the dimension of the continuus time flow.

Commentary

Remark 4.1 Singular value decomposition of Jacobian matrix. For a discussion of the singular value decomposition (SVD) of Jacobian matrix, see for example Thiffeault [4.1].

Remark 4.2 Kuramoto-Sivashinsky system, truncations. We describe here our criterion for reliable truncations of the infinite ladder of ordinary differential equations (2.19).

Adding an extra dimension to a truncation of the system (2.19) introduces a small perturbation, and this can (and often will) throw the system into a totally different asymptotic state. A chaotic attractor for $N = 15$ can become a period three window for $N = 16$, and so on. If we compute, for example, the Lyapunov exponent $\lambda(\nu, N)$ for the strange attractor of the system (2.19), there is no reason to expect $\lambda(\nu, N)$ to smoothly converge to the limit value $\lambda(\nu, \infty)$ as $N \to \infty$. The situation is different in the periodic windows, where the system is structurally stable, and it makes sense to compute Lyapunov exponents, escape rates, etc. for the *repeller*, that is, the closure of the set of all *unstable* periodic orbits. Here the power of cycle expansions comes in: to compute quantities on the repeller by direct averaging methods is generally more difficult, because the motion quickly collapses to the stable cycle.

Résumé

A neighborhood of a trajectory deforms as it is transported by a flow. In the linear approximation, the matrix of variations $\mathbf{A}$ describes the shear-

$\tilde{p}$	p	$\mathbf{g}_{\tilde{p}}$
0	1 2	σ_{12}
1	1 2 3	C_3
01	12 13	σ_{23}
001	121 232 313	C_3
011	121 323	σ_{13}
0001	1212 1313	σ_{23}
0011	1212 3131 2323	C_3^2
0111	1213 2123	σ_{12}
00001	12121 23232 31313	C_3
00011	12121 32323	σ_{13}
00101	12123 21213	σ_{12}
00111	12123	e
01011	12131 23212 31323	C_3
01111	12132 13123	σ_{23}

$\tilde{p}$	p	$\mathbf{g}_{\tilde{p}}$
000001	121212 131313	σ_{23}
000011	121212 313131 232323	C_3^2
000101	121213	e
000111	121213 212123	σ_{12}
001011	121232 131323	σ_{23}
001101	121231 323213	σ_{13}
001111	121231 232312 313123	C_3
010111	121312 313231 232123	C_3^2
011111	121321 323123	σ_{13}
0000001	1212121 2323232 3131313	C_3
0000011	1212121 3232323	σ_{13}
0000101	1212123 2121213	σ_{12}
0000111	1212123	e
$\cdots$	$\cdots$	$\cdots$

Rossler@R“”ossler system

Table 11.2: C_{3v} correspondence between the binary labeled fundamental domain prime cycles $\tilde{p}$ and the full 3-disk ternary labeled cycles p, together with the C_{3v} transformation that maps the end point of the $\tilde{p}$ cycle into the irreducible segment of the p cycle, see sect. 22.2.2. Breaks in the ternary sequences mark repeats of the irreducible segment. The degeneracy of p cycle is $m_p = 6n_{\tilde{p}}/n_p$. The shortest pair of the fundamental domain cycles related by time reversal (but no spatial symmetry) are the 6-cycles $\overline{001011}$ and $\overline{001101}$.

disks and ignore the escapees. So a typical dynamical system that we care about is *bounded*. If the price for keeping going is high - for example, we try to stir up some tar, and observe it come to a dead stop the moment we cease our labors - the dynamics tends to settle into a simple limiting state. However, as the resistance to change decreases - the tar is heated up and we are more vigorous in our stirring - the dynamics becomes unstable.

If a flow is locally unstable but globally bounded, any open ball of initial points will be stretched out and then folded back.

At this juncture we show how this works on the simplest example: unimodal mappings of the interval. The erudite reader should skim through this chapter and then take a more demanding path, via the Smale horseshoes of chapter 12. Unimodal maps are easier, but physically less motivated. The Smale horseshoes are the high road, more complicated, but the right tool to generalize what we learned from the 3-disk dynamics, and begin analysis of general dynamical systems. It is up to you - unimodal maps suffice to get quickly to the heart of this treatise.

insert into figure 11.8: This unimodal map is an approximation to the repeller given in figure 17.2.

11.3.1 Temporal ordering: itineraries

In this section we learn how to *name* (and, in chapter 13, how to *count*) periodic orbits for the simplest, and nevertheless very instructive case, for 1-dimensional maps of an interval.

link to Rössler examples

Suppose that the compression of the folded interval in figure 11.7 is so fierce that we can neglect the thickness of the attractor. For example, the Rössler flow (2.12) is volume contracting, and an interval transverse to the attractor is stretched, folded and pressed back into a nearly 1-dimensional

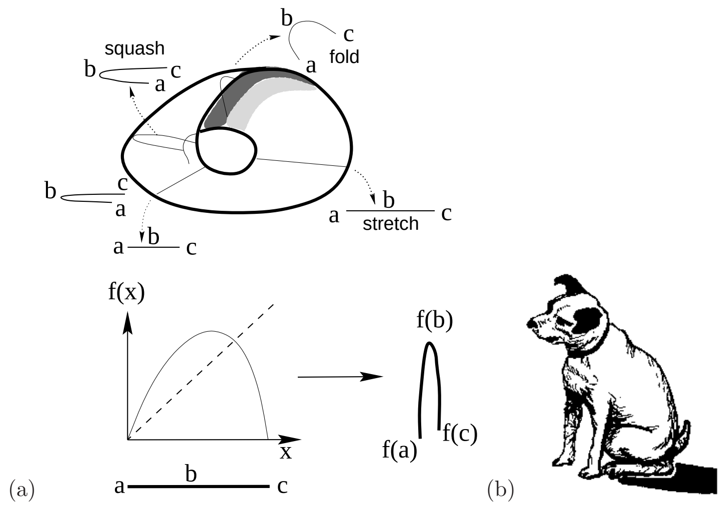

Figure 11.7: (a) A recurrent flow that stretches and folds. (b) The “stretch & fold” return map on the Poincaré section.

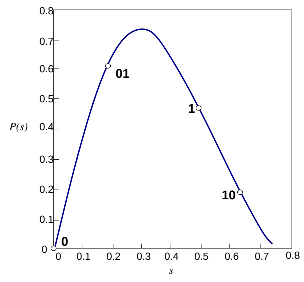

Figure 11.8: The Poincaré return map of the Kuramoto-Sivashinsky system (2.19) figure 3.3, from the unstable manifold of the $\overline{1}$ fixed point to the (neighborhood of) the unstable manifold. Also indicated are the periodic points $\overline{0}$ and $\overline{01}$.

Smale, S.
Kuramoto-Sivashinsky system

Chapter 12

Qualitative dynamics, for cyclists

> **I.1. Introduction to conjugacy problems for diffeomorphisms.** This is a survey article on the area of global analysis defined by differentiable dynamical systems or equivalently the action (differentiable) of a Lie group G on a manifold M. Here Diff(M) is the group of all diffeomorphisms of M and a diffeomorphism is a differentiable map with a differentiable inverse. (...) Our problem is to study the global structure, that is, all of the orbits of M.
> Stephen Smale, *Differentiable Dynamical Systems*

In sects. 9.1 and 11.1 we introduced the concept of partitioning the phase space, in any way you please. In chapter 8 we established that stability eigenvalues of periodic orbits are invariants of a given flow. The invariance of stabilities of a periodic orbit is a local property of the flow.

Both in the Rössler flow of example 3.3, and in the Kuramoto-Sivashinsky system of example 3.4 we have learned that the attractor is very thin, but otherwise the return maps that we found were disquieting – neither figure 3.2 nor figure 3.3 appeared to be one-to-one maps. This apparent loss of invertibility is an artifact of projection of higher-dimensional return maps onto lower-dimensional subspaces. As the choice of lower-dimensional subspace is arbitrary, the resulting snapshots of return maps look rather arbitrary, too. Other projections might look even less suggestive.

needs expanding!

Such observations beg a question: Does there exist a "natural", intrinsically optimal coordinate system in which we should plot of a return map?

explain return map here

As we shall now argue (see also sect. 17.1), the answer is yes: The intrinsic coordinates are given by the stable/unstable manifolds, and a return map should be plotted as a map from the unstable manifold back onto the immediate neighborhood of the unstable manifold.

In this chapter we show that every equilibrium point and every peri-

stable!manifold
unstable!manifold
manifold!stable
stable!manifold!flow
unstable!manifold, flow
stable!manifold!map
unstable!manifold!map

odic orbit carries with it stable and unstable manifolds which provide a topologically invariant *global* foliation of the phase space. This qualitative dynamics of stretching and mixing enables us to partition the phase space and assign symbolic dynamics itineraries to trajectories.

Given an itinerary, the topology of stretching and folding fixes the relative spatial ordering of trajectories, and separates the admissible and inadmissible itineraries. The level is distinctly cyclist, in distincition to the pedestrian tempo of the preceeding chapter. Skip this chapter unless you really need to get into nitty-gritty details of symbolic dynamics.

fast track:
chapter 13, p. 219

12.1 Going global: Stable/unstable manifolds

A neighborhood of a trajectory deforms as it is transported by the flow. In the linear approximation, the matrix of variations A describes this shearing of an infinitesimal neighborhood in an infinitesimal time step. The shearing after finite time is described by the Jacobian matrix $\mathbf{J}^t$. Its eigenvalues and eigendirections describe deformation of an initial infinitesimal sphere of neighboring trajectories into an ellipsoid time t later. Nearby trajectories separate exponentially along the unstable directions, approach each other along the stable directions, and maintain their distance along the marginal directions.

The fixed or periodic point x^* stability matrix $\mathbf{J}_p(x^*)$ eigenvectors (8.9) form a rectilinear coordinate frame in which the flow into, out of, or encircling the fixed point is linear in the sense of sect. 4.2. These eigendirections are numerically continued into global curvilinear invariant manifolds as follows.

The global continuations of the local stable, unstable eigendirections are called the *stable*, respectively *unstable manifolds*. They consist of all points which march into the fixed point forward, respectively backward in time

$$\begin{aligned} W^s &= \left\{x \in \mathcal{M} : f^t(x) - x^* \to 0 \text{ as } t \to \infty\right\} \\ W^u &= \left\{x \in \mathcal{M} : f^{-t}(x) - x^* \to 0 \text{ as } t \to \infty\right\} . \end{aligned} \tag{12.1}$$

The stable/unstable manifolds of a flow are rather hard to visualize, so as long as we are not worried about a global property such as the number of times they wind around a periodic trajectory before completing a parcourse, we might just as well look at their Poincaré section return maps. Stable, unstable manifolds for maps are defined by

define y^*; note 2-dimensional only example

$$\begin{aligned} W^s &= \left\{x \in \mathcal{P} : f^n(x) - x^* \to 0 \text{ as } n \to \infty\right\} \\ W^u &= \left\{x \in \mathcal{P} : f^{-n}(x) - x^* \to 0 \text{ as } n \to \infty\right\} . \end{aligned} \tag{12.2}$$

For $n \to \infty$ any finite segment of W^s, respectively W^u converges to the linearized map eigenvector $\mathbf{e}^{(e)}$, respectively $\mathbf{e}^{(c)}$. In this sense each eigenvector defines a (curvilinear) axis of the stable, respectively unstable manifold.

Conversely, we can use an arbitrarily small segment of a fixed point eigenvector to construct a finite segment of the associated manifold. Precise construction depends on the type of the eigenvalue(s).

Expanding real and positive eigendirection. Consider ith expanding eigenvalue, eigenvector pair $(\Lambda_i, \mathbf{e}_i)$ computed from $\mathbf{J}$ evaluated at a cycle point,

$$\mathbf{J}(x)\mathbf{e}_i(x) = \Lambda_i \mathbf{e}_i(x)\,, \quad x \in p\,, \quad \Lambda_i > 1\,. \tag{12.3}$$

Take an infinitesimal eigenvector $\epsilon\,\mathbf{e}_i(x)$, $\epsilon \ll 1$, and its image $\mathbf{J}_p(x)\epsilon\,\mathbf{e}_i(x) = \Lambda_i\epsilon\,\mathbf{e}_i(x)$. Sprinkle the interval $|\Lambda_i - 1|\epsilon$ with a large number of points x_m, equidistantly spaced on logarithmic scale $\ln|\Lambda_i - 1| + \ln\epsilon$. The successive images of these points $f(x_j)$, $f^2(x_j)$, $\cdots$, $f^m(x_j)$ trace out the curvilinear unstable manifold in direction $\mathbf{e}_i$. Repeat for $-\epsilon\,\mathbf{e}_i(x)$.

Contractiong real, positive eigendirection. Reverse the action of the map backwards in time. This turns a contracting direction into an expanding one, tracing out the curvilinear stable manifold in continuation of $\epsilon\,\mathbf{e}_j$.

Expanding/contracting real negative eigendirection. As above, but every even iterate $f^2(x_j)$, $f^4(x_j)$, $f^6(x_j)$ continues in the direction $\mathbf{e}_i$, every odd one in the direction $-\mathbf{e}_i$.

Complex eigenvalue pair. Construct an orthonormal pair of eigenvectors spanning the plane $\{\epsilon\,\mathbf{e}_j, \epsilon\,\mathbf{e}_{j+1}\}$. Iteration of the annulus between an infinitesimal circle and its image by $\mathbf{J}$ spans the spiralling/circle unstable manifold of the complex eigenvalue pair $\{\Lambda_i, \Lambda_{i+1} = \Lambda_i^*\}$.

⇓PRELIMINARY

Alternatively, one can write down a parametric equation for the stable (unstable) manifold and generate the manifold by integrating the equation.

explain, draw figure

⇑PRELIMINARY

12.2 Horseshoes

If a flow is locally unstable but globally bounded, any open ball of initial points will be stretched out and then folded back. An example is a 3-dimensional invertible flow sketched in figure 11.7 which returns an area of a Poincaré section of the flow stretched and folded into a "horseshoe", such that the initial area is intersected at most twice(see figure 12.4). Run backwards, the flow generates the backward horseshoe which intersects the forward horseshoe at most 4 times, and so forth. Such flows exist, and

⇓PRIVATE

⇑PRIVATE

motivate 1-d maps with this, replace figure 11.7 by hand-drawn version

Rossler@R"'ossler system
horseshoe
map!once-folding
Poincar"'e!section
return map
map!return
Henon@H"'enon!map
Henon@H"'enon!map!fixed points
Add Predrag's pictures
Henon@H"'enon!map!inverse
stable!manifold
unstable!manifold
3.4 page 64
make example for negative b?

are easily constructed - an example is the Rössler system , discussed in example 3.3.

Now we shall construct an example of a locally unstable but globally bounded mapping which returns an initial area stretched and folded into a "horseshoe", such that the initial area is intersected at most twice. We shall refer to such mappings with at most 2^n transverse self-intersections at the nth iteration as the *once-folding* maps.

12.1 page 214

As an example is afforded by the 2-dimensional *Hénon map*

$$\begin{aligned} x_{n+1} &= 1 - a x_n^2 + b y_n \\ y_{n+1} &= x_n\,. \end{aligned} \tag{12.4}$$

The Hénon map models qualitatively the Poincaré section return map of figure 11.7. For $b = 0$ the Hénon map reduces to the parabola (11.9), and, as shown in sects. 3.4 and 33.1, for $b \neq 0$ it is kind of a fattened parabola; by construction, it takes a rectangular initial area and returns it bent as a horseshoe.

For definitiveness, fix the parameter values to $a = 6$, $b = 0.9$. The map is quadratic, so it has 2 fixed points $x_0 = f(x_0)$, $x_1 = f(x_1)$ indicated in figure 12.1 (a). For the parameter values at hand, they are both unstable.

add exercise

If you start with a small ball of initial points centered around x_1, and iterate the map, the ball will be stretched and squashed along the line W_1^u.
Similarly, a small ball of initial points centered around the other fixed point x_0 iterated backward in time,

$$\begin{aligned} x_{n-1} &= y_n \\ y_{n-1} &= -\frac{1}{b}(1 - a y_n^2 - x_n)\,, \end{aligned} \tag{12.5}$$

sect?

traces out the line W_0^s. W_0^s is the stable manifold of x_0 fixed point, and W_1^u is the unstable manifold of x_1 fixed point, defined in sect. 12.1. Their intersections enclose the crosshatched region $\mathcal{M}_.$. Any point outside W_1^u border of $\mathcal{M}_.$ escapes to infinity forward in time, while any point outside W_0^s border escapes to infinity backwards in time. In this way the unstable - stable manifolds define topologically, invariant and optimal $\mathcal{M}_.$ initial region; all orbits that stay confined for all times are confined to $\mathcal{M}_.$.

Iterated one step forward, the region $\mathcal{M}_.$ is stretched and folded into a *smale* horseshoe drawn in figure 12.1 (b). The horseshoe fattened parabolla shape is the consequence og the quadratic form x^2 in (12.4). Parameter a controls the amount of stretching, while the parameter b controls the amount of compression of the folded horseshoe. The case $a = 6$, $b = 0.9$ considered here corresponds to strong stretching and weak compression. Label the two forward intersections $f(\mathcal{M}_.) \cap \mathcal{M}_.$ by $\mathcal{M}_{s.}$, with $s \in \{0, 1\}$, figure 12.1 (b). The horseshoe consists of the two strips $\mathcal{M}_{0.}, \mathcal{M}_{1.}$, and the bent segment that lies entirely outside the W_1^u line. As all points in this

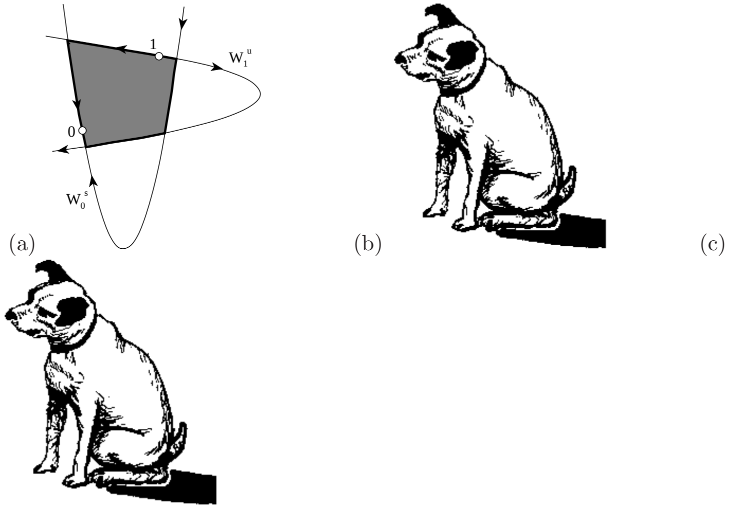

Figure 12.1: The Hénon map for $a = 6$, $b = .9$. (a) The fixed points $\overline{0}$, $\overline{1}$, and the segments of the W_0^s stable manifold, W_1^u unstable manifold that enclose the initial (crosshatched) region $\mathcal{M}_.$. (b) The forward horseshoe $f(\mathcal{M}_.)$. (c) The backward horseshoe $f^{-1}(\mathcal{M}_.)$. Iteration yields a complete Smale horseshoe, with every forward fold intersecting every backward fold.

con-
ation,

segment escape to infinity under forward iteration, this region can safely be cut out and thrown away.

Iterated one step backwards, the region $\mathcal{M}_.$ is again stretched and folded into a horseshoe, figure 12.1 (c). As stability and instability are interchanged under time reversal, this horseshoe is transverse to the forward one. Again the points in the horseshoe bend wonder off to infinity as $n \to -\infty$, and we are left with the two (backward) strips $\mathcal{M}_{.0}, \mathcal{M}_{.1}$. Iterating two steps forward we obtain the four strips $\mathcal{M}_{11.}, \mathcal{M}_{01.}, \mathcal{M}_{00.}, \mathcal{M}_{10.}$, and iterating backwards we obtain the four strips $\mathcal{M}_{.00}, \mathcal{M}_{.01}, \mathcal{M}_{.11}, \mathcal{M}_{.10}$ transverse to the forward ones just as for 3-disk pinball game figure 11.3. Iterating three steps forward we get an 8 strips, and so on *ad infinitum*.

What is the significance of the subscript $_{.011}$ which labels the $\mathcal{M}_{.011}$ backward strip? The two strips $\mathcal{M}_{.0}, \mathcal{M}_{.1}$ partition the phase space into two regions labeled by the two-letter alphabet $\mathcal{A} = \{0, 1\}$. $S^+ = .011$ is the *future itinerary* for all $x \in \mathcal{M}_{.011}$. Likewise, for the forward strips all $x \in \mathcal{M}_{s_{-m}\cdots s_{-1}s_0.}$ have the *past itinerary* $S^- = s_{-m}\cdots s_{-1}s_0$. Which partition we use to present pictorially the regions that do not escape in m iterations is a matter of taste, as the backward strips are the preimages of the forward ones

$$\mathcal{M}_{0.} = f(\mathcal{M}_{.0}) , \qquad \mathcal{M}_{1.} = f(\mathcal{M}_{.1}) .$$

Ω, the non–wandering set (2.2) of $\mathcal{M}_.$, is the union of all points whose

non-wandering set
set!non-wandering
symbolic dynamics!complete
structural stability
stability!structural
horseshoe!complete
structural stability
stability!structural
ordering!spatial

forward and backward trajectories remain trapped for all time. given by the intersections of all images and preimages of $\mathcal{M}$:

$$\Omega = \left\{ x : x \in \lim_{m,n\to\infty} f^m(\mathcal{M}_.) \bigcap f^{-n}(\mathcal{M}_.) \right\} . \qquad (12.6)$$

Two important properties of the Smale horseshoe are that it has a *complete binary symbolic dynamics* and that it is *structurally stable*.

For a *complete* Smale horseshoe every forward fold $f^n(\mathcal{M})$ intersects transversally every backward fold $f^{-m}(\mathcal{M})$, so a unique bi-infinite binary sequence can be associated to every element of the non–wandering set. A point $x \in \Omega$ is labeled by the intersection of its past and future itineraries $S(x) = \cdots s_{-2}s_{-1}s_0.s_1s_2\cdots$, where $s_n = s$ if $f^n(x) \in \mathcal{M}_{.s}$, $s \in \{0, 1\}$ and $n \in \mathbb{Z}$. For sufficiently separated disks, the 3-disk game of pinball figure 11.3, is another example of a complete Smale horseshoe; in this case the "folding" region of the horseshoe is cut out of the picture by allowing the pinballs that fly between the disks to fall off the table and escape.

The system is said to be *structurally stable* if all intersections of forward and backward iterates of $\mathcal{M}$ remain transverse for sufficiently small perturbations $f \to f + \delta$ of the flow, for example, for slight displacements of the disks, or sufficiently small variations of the Hénon map parameters a, b while structural stability is exceedingly desirable, it is also exceedingly rare. About this, more later.

⇓PRELIMINARY

Inspecting the figure 12.1 (c) we see that the relative ordering of regions with differing finite itineraries is a qualitative, topological property of the flow, so it makes sense to define a simple "canonical" representative partition for the entire class of topologically similar flows.

⇑PRELIMINARY

12.3 Spatial ordering

Consider a system for which you have succeeded in constructing a covering symbolic dynamics, such as a well-separated 3-disk system. Now start moving the disks toward each other. At some critical separation a disk will start blocking families of trajectories traversing the other two disks. The order in which trajectories disappear is determined by their relative ordering in space; the ones closest to the intervening disk will be pruned first. Determining inadmissible itineraries requires that we relate the spatial ordering of trajectories to their time ordered itineraries.

12.9
page 217

So far we have rules that, given a phase space partition, generate a *temporally* ordered itinerary for a given trajectory. Our next task is the reverse: given a set of itineraries, what is the *spatial* ordering of corresponding points along the trajectories? In answering this question we will be aided by Smale's visualization of the relation between the topology of a flow and its symbolic dynamics by means of "horseshoes".

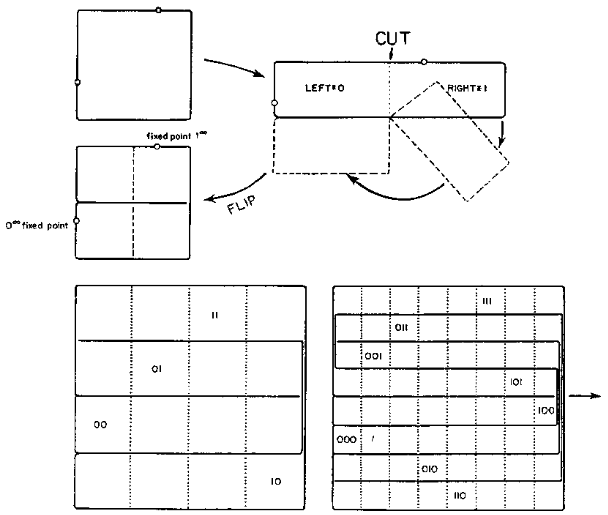

symbol plane@"topp
symbol!square
rectangle
symbol plane@"topp

Figure 12.2: Kneading Danish Pastry: symbol square representation of an orientation reversing once-folding map obtained by fattening the Smale horseshoe intersections of figure 12.1 into a unit square. In the symbol square the dynamics maps rectangles into rectangles by a decimal point shift.

12.3.1 Symbol square

complement figure 12.2 with a figure of rectangles mapping into rectangles

say symbol square is a product of two tent maps

rescan the knife into figure 12.2

For a better visualization of 2-dimensional non–wandering sets, fatten the intersection regions until they completely cover a unit square, as in figure 12.2. We shall refer to such a "map" of the topology of a given "stretch & fold" dynamical system as the *symbol square*. The symbol square is a topologically accurate representation of the non–wandering set and serves as a street map for labeling its pieces. Finite memory of m steps and finite foresight of n steps partitions the symbol square into *rectangles* $[s_{-m+1}\cdots s_0.s_1s_2\cdots s_n]$. In the binary dynamics symbol square the size of such rectangle is $2^{-m}\times 2^{-n}$; it corresponds to a region of the dynamical phase space which contains all points that share common n future and m past symbols. This region maps in a nontrivial way in the phase space, but in the symbol square its dynamics is exceedingly simple; all of its points are mapped by the decimal point shift (11.20)

12.2 page 214

$$\sigma(\cdots s_{-2}s_{-1}s_0.s_1s_2s_3\cdots) = \cdots s_{-2}s_{-1}s_0s_1.s_2s_3\cdots\,, \tag{12.7}$$

For example, the square [01.01] gets mapped into the rectangle $\sigma[01.01] =$ [010.1], see figure 12.4 (b).

⇓PRELIMINARY
⇑PRELIMINARY

draw a better figure!

As the horseshoe mapping is a simple repetitive operation, we expect a simple relation between the symbolic dynamics labeling of the horseshoe strips, and their relative placement. The symbol square points $\gamma(S^+)$ with

12.3 page 214

12.4 page 215

past "topc

future itinerary S^+ are constructed by converting the sequence of s_n's into a binary number by the algorithm (??). This follows by inspection from figure 12.2. In order to understand this relation between the topology of horseshoes and their symbolic dynamics, it might be helpful to backtrace to sect. 11.3.2 and work through and understand first the symbolic dynamics of one-dimensional unimodal mappings.

into exercises - orientation preserving case

Under backward iteration the roles of 0 and 1 symbols are interchanged; $\mathcal{M}_0^{-1}$ has the same orientation as $\mathcal{M}$, while $\mathcal{M}_1^{-1}$ has the opposite orientation. We assign to an *orientation preserving* once-folding map the *past topological coordinate* $\delta = \delta(S^-)$ by the algorithm:

12.5 page 215

recheck this

$$\begin{aligned} w_{n-1} &= \begin{cases} w_n & \text{if } s_n = 0 \\ 1-w_n & \text{if } s_n = 1 \end{cases}\,, \qquad w_0 = s_0 \\ \delta(S^-) &= 0.w_0w_{-1}w_{-2}\ldots = \sum_{n=1}^{\infty} w_{1-n}/2^n\,. \end{aligned} \tag{12.8}$$

Such formulas are best derived by quiet contemplation of the action of a folding map, in the same way we derived the future topological coordinate (??).

The coordinate pair (δ,γ) maps a point (x,y) in the phase space Cantor set of figure 12.1 into a point in the symbol square of figure 12.2, preserving the topological ordering; (δ,γ) serves as a topologically faithful representation of the non–wandering set of any once-folding map, and aids us in partitioning the set and ordering the partitions for any flow of this type.

Include results of refs. [12.65, 12.66]

add chapter on templates, braids?

12.4 Pruning

> The complexity of this figure will be striking, and I shall not even try to draw it.
>
> H. Poincaré, on his discovery of homoclinic tangles,
> *Les méthodes nouvelles de la méchanique céleste*

In general, not all possible itineraries are realized as physical trajectories. Trying to get from "here" to "there" we might find that a short path is excluded by some obstacle, such as a disk that blocks the path, or a potential ridge. To count correctly, we need to *prune* the inadmissible trajectories, that is, specify the grammar of the admissible itineraries.

While the complete Smale horseshoe dynamics discussed so far is rather straightforward, we had to get through it in order to be able to approach a situation that resembles more the real life: adjust the parameters of a once-folding map so that the intersection of the backward and forward folds is still transverse, but no longer complete, as in figure 13.2 (a). The utility of the symbol square lies in the fact that the surviving, admissible itineraries still maintain the same relative spatial ordering as for the complete case.

replace by the Biham Hénon example

add Henon exercise based on AACI, AACII

Chapter 17

Fixed points, and how to get them

periodic!orbit extraction—(
periodic!orbit condition
prime cycle
cycle!prime
fixed point
cyclic!invariance
invariance!cyclic

(F. Christiansen)

Having set up the dynamical context, now we turn to the key and unavoidable piece of numerics in this subject; search for the solutions (x, T), $x \in \mathbb{R}^d$, $T \in \mathbb{R}$ of the *periodic orbit condition*

$$f^{t+T}(x) = f^t(x)\,, \qquad T > 0 \tag{17.1}$$

for a given flow or mapping.

We know from chapter 14 that cycles are the necessary ingredient for evaluation of spectra of evolution operators. In chapter 11 we have developed a qualitative theory of how these cycles are laid out topologically. This chapter is intended as a hands-on guide to extraction of periodic orbits, and should be skipped on first reading - you can return to it whenever the need for finding actual cycles arises. A serious cyclist might want to also learn about the variational methods to find cycles, chapter 33. They are particularly useful when little is understood about the topology of a flow, such as in high-dimensional periodic orbit searches.

chapter 33

fast track:
chapter 18, p. 331

A *prime* cycle p of period T_p is a single traversal of the periodic orbit, so our task will be to find a cycle point $x \in p$ and the shortest time T_p for which (17.1) has a solution. A cycle point of a flow f^t which crosses a Poincaré section n_p times is a fixed point of the P^{n_p} iterate of the Poincaré section return map P, hence we shall refer to all cycles as "fixed points" in this chapter. By cyclic invariance, stability eigenvalues and the period of the cycle are independent of the choice of the initial point, so it will suffice to solve (17.1) at a single cycle point.

sect. 8.2

Rossler@Rössler system!cycles
cycle!Rössler system

If the cycle is an attracting limit cycle with a sizable basin of attraction, it can be found by integrating the flow for sufficiently long time. If the cycle is unstable, simple integration forward in time will not reveal it, and methods to be described here need to be deployed. In essence, any method for finding a cycle is based on devising a new dynamical system which possesses the same cycle, but for which this cycle is attractive. Beyond that, there is a great freedom in constructing such systems, and many different methods are used in practice.

Due to the exponential divergence of nearby trajectories in chaotic dynamical systems, fixed point searches based on direct solution of the fixed-point condition (17.1) as an initial value problem can be numerically very unstable. Methods that start with initial guesses for a number of points along the cycle, such as the multipoint shooting method described here in sect. 17.3, and the variational) methods of chapter 33, are considerably more robust and safer.

chapter 33

A prerequisite for any exhaustive cycle search is a good understanding of the topology of the flow: a preliminary step to any serious periodic orbit calculation is preparation of a list of all distinct admissible prime periodic symbol sequences, such as the list given in table 11.1. The relations between the temporal symbol sequences and the spatial layout of the topologically distinct regions of the phase space discussed in chapters 11 and 12 should enable us to guess location of a series of periodic points along a cycle. Armed with such informed guess we proceed to improve it by methods such as the Newton-Raphson iteration; we illustrate this by considering 1-dimensional and d-dimensional maps.

perhaps include also Kai's method

17.1 Where are the cycles?

Ergodic exploration of recurrences that we turn to now sometimes performs admirably well in getting us started.

emphasize importance of equilibrium points!

Both in the example of the Rössler flow and of the Kuramoto-Sivashinsky system we sketched the attractors by running a long chaotic trajectory, and noted that the attractors are very thin, but otherwise the return maps that we plotted were disquieting – neither figure 3.2 nor figure 3.3 appeared to be 1-to-1 maps. In this section we show how to use such information to approximately locate cycles. In the remainder of this chapter and in chapter 33 we shall learn how to turn such guesses into highly accurate cycles.

Example 17.1 Rössler attractor *(G. Simon and P. Cvitanović)*

Run a long simulation of the Rössler flow f^t, plot a Poincaré section, as in figure 3.1, and extract the corresponding Poincaré return map P, as in figure 3.2. Luck is with us; the figure 17.1(a) return map $y \to P_1(y, z)$ looks much like a parabola, so we take the unimodal map symbolic dynamics, sect. 11.3.1, as our guess for the covering dynamics. Strictly speaking, the attractor is "fractal", but for all practical purposes the return map

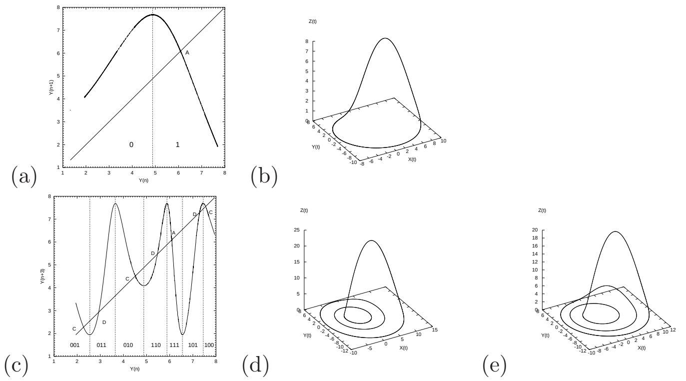

Figure 17.1: (a) $y \to P_1(y,z)$ return map for $x=0$, $y>0$ Poincaré section of the Rössler flow figure 2.3. (b) The $\overline{1}$-cycle found by taking the fixed point $y_{k+n} = y_k$ together with the fixed point of the $z \to z$ return map (not shown) an initial guess $(0, y^(0), z^(0))$ for the Newton-Raphson search. (c) $y_{k+3} = P_1^3(x_k, y_k)$, the third iterate of Poincaré return map (3.1) together with the corresponding plot for $z_{k+3} = P_2^3(x_k, y_k)$, is used to pick starting guesses for the Newton-Raphson searches for the two 3-cycles: (d) the $\overline{001}$ cycle, and (e) the $\overline{011}$ cycle. (G. Simon)

is 1-dimensional; your printer will need a resolution better than 10^{14} dots per inch to start resolving its structure.

Periodic points of a prime cycle p of cycle length n_p for the $x=0$, $y>0$ Poincaré section of the Rössler flow figure 2.3 are fixed points $(y,z) = Pn(y,z)$ of the nth Poincaré return map.

Using the fixed point $y_{k+1} = y_k$ in figure 17.1(a) together with the simultaneous fixed point of the $z \to P_1(y,z)$ return map (not shown) as a starting guess $(0, y^{(0)}, z^{(0)})$ for the Newton-Raphson search for the cycle p with symbolic dynamics label $\overline{1}$, we find the cycle figure 17.1(b) with the Poincaré section point $(0, y_p, z_p)$, period T_p, expanding, marginal, contracting stability eigenvalues $(\Lambda_{p,e}, \Lambda_{p,m}, \Lambda_{p,c})$, and Lyapunov exponents $(\lambda_{p,e}, \lambda_{p,m}, \lambda_{p,c})$:

$$
\begin{array}{lrcl}
\overline{1}\text{-cycle:} & (x,y,z) & = & (0, 6.09176832, 1.2997319) \\
 & T_1 & = & 5.88108845586 \\
 & (\Lambda_{1,e}, \Lambda_{1,m}, \Lambda_{1,c}) & = & (-2.40395353, 1 + 10^{-14}, -1.29 \times 10^{-14}) \\
 & (\lambda_{1,e}, \lambda_{1,m}, \lambda_{1,c}) & = & (0.149141556, 10^{-14}, -5.44)\,. \qquad (17.2)
\end{array}
$$

The Newton-Raphson method that we used is described in sect. 17.5.

17.8 page 329

As an example of a search for longer cycles, we use $y_{k+3} = P^3(y_k, z_k)$, the third iterate of Poincaré return map (3.1) plotted in figure 17.1(c), together with a corresponding plot for $z_{k+3} = f^3(y_k, z_k)$, to pick starting guesses for the Newton-Raphson searches for the two 3-cycles plotted in figure 17.1(d), (e). For a listing of the short cycles of the Rössler flow, consult table 17.1.

recheck $\Lambda_c = -1.29 \times 10^{-14}$

The numerical evidence suggests (but a proof is lacking) that all cycles that comprise the strange attractor of the Rössler system are hyperbolic, each with an expanding eigenvalue $|\Lambda_e| > 1$, a contracting eigenvalue $|\Lambda_c| < 1$, and a marginal eigenvalue $|\Lambda_m| = 1$ corresponding to displacements along the direction of the flow.

For the Rössler system the contracting eigenvalues turn out to be insanely contracting, a factor of e^{-32} per one par-course of the attractor, so their numerical

template Kuramoto-Sivashinsky system

determination is quite difficult. Fortunately, they are irrelevant; for all practical purposes the strange attractor of the Rössler system is 1-dimensional, a very good realization of a horseshoe template.

⇓PRELIMINARY

The next example will have a thicker attractor. By the time you have to deal with extended fractal attractors, such as the Hénon map attractor plotted in figure 3.4, or Hamiltonian strange sets, you will develop deep respect for the gymnastics of qualitative dynamics, chapters 11 and 12. Of course, the initial guesses are worth naught until you have mastered the numerical techniques of the remainder of this chapter.

Example 17.2 Kuramoto-Sivashinsky system. *In sect. 20.1 we have developed basic understanding of [1] The full return map is $(N-1)$-dimensional $\mathbf{a} \to \mathbf{P}(a_2, \ldots, a_N) = \mathbf{a}'$ and single-valued, and for the examples considered the attractor is essentially 1-dimensional, but its projection into the $\{a_k, P_k(a_2, \ldots, a_N)\}$ plane, a return map for a given coordinate $a_k \to a'_k = P_k(a_2, \ldots, a_N)$ can appear multi-valued and self-intersecting. The multiple-valuedness in figure 3.3 arises from the fact that the return map is a 2-dimensional projection of a convoluted 1-dimensional curve embedded into a high-dimensional space. One can imagine a situation where no "good" projection is possible, that is, any projection onto any 2-dimensional plane is a multiple-valued function. The question is: does there exist an intrinsically optimal representation of a return map? and the answer is, yes, the intrinsic coordinates are given by the stable/unstable manifolds, and a return map should be plotted as a map from the unstable manifold back onto the unstable manifold.*

reminder should go to the fixed points chapter

We now show how this works for the Kuramoto-Sivashinsky example. We shall show that it is possible to find an intrinsic *parametrization s along the unstable manifold, such that the map $s \to f(s)$ induced by the full d-dimensional flow is approximately 1-dimensional. Strictly speaking, the attractor on figure 3.3 has a certain thickness transverse to it, but the contraction in the transverse directions is so strong that the invariant set is effectively 1-dimensional.*

Suppose we already have determined some of the shorter cycles for our system, that is, the fixed points of the Poincaré map and its iterates. This is accomplished relatively easily by checking a trajectory of a random initial point for close returns and then using these as initial guesses for a cycle search algorithm. We now assume that the invariant set can be approximated by a curve passing close to all periodic points, and determine the order of periodic points along such curve. This is done in the following way: there exists a fixed point which is not connected to the attractor (the point $\overline{0}$ in figure 3.3) - we choose this fixed point as the starting point and assign it number 1. Point number 2 is the periodic point in the sample which is closest (in the full space) to this fixed point, and the nth point is determined as the point which has the minimum distance from the point number $n-1$ among all the periodic points which have not yet been enumerated. Proceeding this way, we order all the periodic points that we have found so far.

Since all periodic points belong to cycles, their images are known and are simply the successive periodic points along the cycle. We use this fact to recursively construct a 1-dimensional mapping $s_i \to f(s_i)$. We approximate parametrization length s along the invariant set by computing the Euclidean inter-distances between the successive periodic points in the full dynamical space, $s_1 = 0, s_2 = \|\mathbf{a}_2 - \mathbf{a}_1\|, s_i - s_{i-1} = \|\mathbf{a}_i - \mathbf{a}_{i-1}\|$. The ith cycle point s_i is mapped onto its image $s_{\sigma i} = f(s_i)$, where σ_i denotes the label of the next periodic point in the cycle. We can now find longer cycles of the 1-dimensional map f by standard methods such as inverse iteration, and guess the location of the corresponding points in the full N-dimensional space by interpolating

[1] Dorte: ulaeseligt

Figure 17.2: The return map $s_{n+1} = f(s_n)$ constructed from the images of periodic points. The diamonds were obtained by using 34 periodic points, the dots were obtained by using 240 periodic points. We have indicated the periodic points $\overline{0}$, $\overline{1}$ and $\overline{01}$. Note that the transverse fractal structure of the map shows when the number of points is increased. $N = 16$ Fourier modes truncation with $\nu = 0.029910$. (From ref. [2.10])

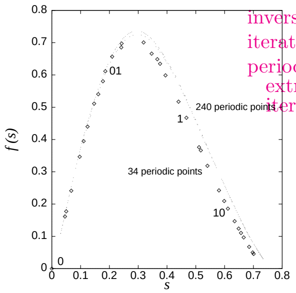

inverse iteration
iteration!inverse
periodic!orbit extraction!inverse iteration

between the nearest known periodic points. These will not be exact cycles of the full system, but are very useful as good starting guesses in a search for the exact cycles. Iteratively, more and more cycles can be computed. While it only pays to refine the 1-dimensional parametrization until the density of the periodic points become so high that the width of the attractor becomes noticeable, the 1-dimensional map continues to provide good initial guesses to longer cycles. More sophisticated methods are needed only if high accuracy around the folding region of $f(s)$ is required in order to distinguish between long cycles.

For the values of ν we are working with, the approximate return map $s \to f(s)$ is unimodal.

We use the unimodal map $s \to f(s)$ to construct binary symbolic dynamics for the system in the usual way: assign the symbol '0' to points to the left of the maximum, '1' to the points to the right. In the period-3 window with the stable cycle $\overline{001}$, the pruning rules are very easy: except for the stable $\overline{001}$ cycle and the $\overline{0}$ fixed point (both disjoint from the invariant set) two 0's in a row are forbidden. In this case it is convenient to redefine the alphabet by denoting the symbol pair 01 by a and the symbol 1 by b. This renders the symbolic dynamics of the points on the repeller complete binary: all sequences of the letters a and b are admissible.

⇑PRELIMINARY

17.2 One-dimensional mappings

17.2.1 Inverse iteration

draw a figure of a unimodal repeller, its inverse

Let us first consider a very simple method to find unstable cycles of a 1-dimensional map such as the logistic map. Unstable cycles of 1-d maps are attracting cycles of the inverse map. The inverse map is not single valued, so at each backward iteration we have a choice of branch to make. By choosing branch according to the symbolic dynamics of the cycle we are trying to find, we will automatically converge to the desired cycle. The rate of convergence is given by the stability of the cycle, that is, the convergence is exponentially fast. Figure 17.3 shows such path to the $\overline{01}$-cycle of the logistic map.

17.12
page 329

The method of inverse iteration is fine for finding cycles for 1-d maps and some 2-d systems such as the repeller of exercise 17.12. It is not particularly fast, especially if the inverse map is not known analytically. However, it completely fails for higher dimensional systems where we have both stable

periodic!orbit extraction!Newton's method—(
Newton's method
periodic!orbit extraction!Newton's method—)
Newton's method!convergence
damped Newton's method
Newton's method!damped

Figure 17.3: The inverse time path to the $\overline{01}$-cycle of the logistic map f(x)=4x(1-x) from an initial guess of x=0.2. At each inverse iteration we chose the 0, respectively 1 branch.

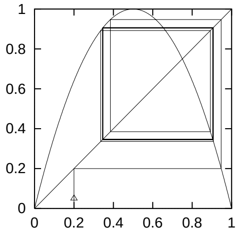

and unstable directions. Inverse iteration will exchange these, but we will still be left with both stable and unstable directions. The best strategy is to directly attack the problem of finding solutions of $f^T(x) = x$.

17.2.2 Newton's method

Newton's method for determining a zero x^* of a function $F(x)$ of one variable is based on a linearization around a starting guess x_0:

$$F(x) \approx F(x_0) + F'(x_0)(x - x_0). \tag{17.3}$$

An approximate solution x_1 of $F(x) = 0$ is

$$x_1 = x_0 - F(x_0)/F'(x_0). \tag{17.4}$$

The approximate solution can then be used as a new starting guess in an iterative process. A fixed point of a map f is a solution to $F(x) = x - f(x) = 0$. We determine x by iterating

$$\begin{aligned} x_m &= g(x_{m-1}) = x_{m-1} - F(x_{m-1})/F'(x_{m-1}) \\ &= x_{m-1} - \frac{1}{1 - f'(x_{m-1})}(x_{m-1} - f(x_{m-1}))\,. \end{aligned} \tag{17.5}$$

Provided that the fixed point is not marginally stable, $f'(x) \neq 1$ at the fixed point x, a fixed point of f is a super-stable fixed point of the Newton-Raphson map g, $g'(x) = 0$, and with a sufficiently good initial guess, the Newton-Raphson iteration will converge super-exponentially fast.

To illustrate the efficiency of the Newton's method we compare it to the inverse iteration method in figure 17.4. Newton's method wins hands down: the number of significant digits of the accuracy of x estimate doubles with each iteration.

In order to avoid jumping too far from the desired x^* (see figure 17.5), one often initiates the search by the *damped Newton's method*,

$$\Delta x_m = x_{m+1} - x_m = -\frac{F(x_m)}{F'(x_m)}\,\Delta\tau\,, \qquad 0 < \Delta\tau \leq 1\,,$$